ORIGINAL PAPER

Magnetic and Microstructural Properties of Nanostructured/Amorphous NiTi Prepared by Mechanical Alloying

Elfahem Sakher[1,2] · Mounir Sakmeche[3] · Billel Smili[1] · Ahmed Bouraiou[4] · Mostepha Benchiheub[5] · Mohamed Bououdina[6] · Stefano Bellucci[7]

Abstract

This study aims to examine the effects of milling time on the morphological, structural, and magnetic properties of nanostructured $Ni_{50}Ti_{50}$ powders prepared by high-energy mechanical alloying using a Fritsch Pulverisette 7 planetary ball mill. Scanning electron microscopy and electron dispersive X-ray spectroscopy, results revealed a novel particle folding phenomenon during high-energy milling, significantly diverging from conventional welding and fracture processes. With increasing milling time, it was observed reduced particle size, and enhanced spherical equiaxial morphology, alongside a mixture of the amorphous phase, NiTi-martensite (Ms), NiTi-austenite (As), and solid solution phases (SS). Rietveld refinements of X-ray diffraction patterns and magnetic measurements highlighted the critical role of the amorphous phase in determining the Ms and Mr values of synthesized $Ni_{50}Ti_{50}$ powders. After 72 h of milling, the coercive field increased to 285.8 Oe, and the martensitic phase proportion reached 21.58%.

1 Introduction

Nickel-titanium (NiTi) alloys have emerged as a versatile class of materials that possess a unique combination of desirable properties, such as shape memory behavior [1], super elasticity [2], good corrosion resistance [3], and biocompatibility [4], making them ideal candidates for a wide range of applications in fields such as biomedical [5], aerospace [6], automotive [7], and robotics [7]. In particular, the excellent biocompatibility and mechanical properties of NiTi alloys make them highly desirable for use in orthopedic [8] and dental implants [9].

✉ Elfahem Sakher
  elf.sakher@univ-adrar.edu.dz

  Mounir Sakmeche
  mounir.sakmeche@univ-adrar.edu.dz

  Billel Smili
  billel.smili@univ-adrar.edu.dz

  Mohamed Bououdina
  mbououdina@psu.edu.sa

  Stefano Bellucci
  stefano.bellucci@lnf.infn.it

1 Laboratory of Energy Environment and Information System (LEEIS), Department of Material Science, Faculty of Science and Technology, University of Adrar, National Highway No. 06, 01000, Adrar, Algeria

2 Environmental Research Center (C.R.E) Sis at Alzone, 23000 Annaba, Algeria

3 Laboratory of Catalytic Materials and Industrial Processes (LMPCI), Department of Hydrocarbons and Renewable Energies, Faculty of Science and Technology, University of Adrar, National Highway No. 06, Adrar 01000, Algeria

4 Centre de Développement des Energies Renouvelables, CDER, Unité de Recherche en Energie Renouvelables en Milieu Saharien, URERMS, 01000 Adrar, Algeria

5 Laboratoire d'Elaboration et d'Analyse des Materiaux LEAM, Department of Physics, Faculty of Science, University Badji Mokhtar, Annaba, Algeria

6 Department of Mathematics and Sciences, Faculty of Humanities and Sciences, Prince Sultan University, Riyadh, Saudi Arabia
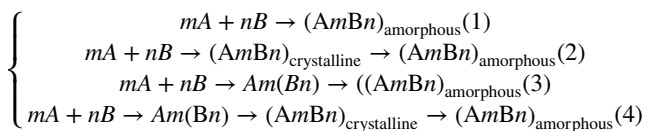
7 INFN-Laboratori Nazionali di Frascati, Via E. Fermi 54, 00044 Frascati, Italy

The properties of NiTi alloys can be significantly enhanced by altering their microstructure, including the amorphization [10] and nanocrystallization [11] processes, which can profoundly impact their electrical [12], mechanical [13], and magnetic [14] properties. Amorphous and nanocrystalline NiTi alloys exhibit unique mechanical properties, such as enhanced strength, toughness, and fatigue resistance, compared to their coarse-grained polycrystalline counterparts [15]. These materials also have the potential to be used in new applications, such as hydrogen storage and catalysis [16].

Several methods have been employed to produce nanocrystalline/amorphous NiTi alloys, including melt-spinning [17], high-pressure torsion [18], self-propagating high-temperature synthesis [19], and mechanical alloying (MA) [20]. Among these, MA has been found as a highly effective method for the preparation of nanocrystalline/ amorphous NiTi alloys [20]. This technique involves repeated cold-welding and fracturing of metallic powders in a ball mill, resulting in a homogeneous distribution of the alloying elements [21].

In the MA process, the reduction of particle size is observed, resulting in ultra-fine-grained materials. This reduction in particle for the preparation of significant improvements in the properties of the materials compared to conventional coarse-grained polycrystalline materials [22].

The amorphization of NiTi alloys by mechanical alloying has been shown to occur via different reaction routes [21, 23]. These routes can result in the direct formation of an amorphous phase or through the formation of an intermetallic or a solid solution phase. These different possibilities may be represented as follows:

$$
\begin{cases}
mA + nB \rightarrow (AmBn)_{\text{amorphous}} & (1) \\
mA + nB \rightarrow (AmBn)_{\text{crystalline}} \rightarrow (AmBn)_{\text{amorphous}} & (2) \\
mA + nB \rightarrow Am(Bn) \rightarrow ((AmBn)_{\text{amorphous}} & (3) \\
mA + nB \rightarrow Am(Bn) \rightarrow (AmBn)_{\text{crystalline}} \rightarrow (AmBn)_{\text{amorphous}} & (4)
\end{cases}
$$

where m and n are the atomic composition of elements A and B, respectively, $Am(Bn)$ represents a solid solution of B in A, $(AmBn)_{\text{crystalline}}$ represents a crystalline phase, and $(AmBn)_{\text{amorphous}}$ represents the amorphous phase with the composition $AmBn$.

Mechanical milling of nickel-titanium (NiTi) shape-memory alloys effectively reduces grain size, enhancing their physicochemical and shape-memory properties [24]. This process focuses on refining milling parameters to maintain the alloys' shape-memory functionality while achieving microstructural improvements, highlighting the potential of NiTi alloys for high-precision applications [25].

This research work presents a comprehensive analysis of the evolution of structural, microstructural, and magnetic properties of nanostructured/amorphous $Ni_{50}Ti_{50}$ alloys

produced via mechanical alloying. Particular emphasis focuses on the influence of processing parameters, including milling time (1 to 72h), milling speed, and the incorporation of alloying elements, on the resulting structural, microstructural, and magnetic characteristics of the milled powders.

2 Experimental Part

High-purity titanium ($> 99\%$, < 150 μm) and nickel ($> 99.5\%$, < 45 μm) powders were purchased from Alfa Aesar GmbH & Co KG for this study. The initial powder mixture had a 50:50 atomic percentage composition of titanium and nickel and was subjected to mechanical alloying using a Fritsch P7 planetary ball mill. An 80-ml tempered steel vial and 15-mm diameter steel balls were employed in the process. Each experimental batch consisted of a 3 g powder mixture, measured using a 3-digit microbalance. The milling took place under an argon atmosphere at a constant speed of 400 rpm and a 23:1 ball-to-powder mass ratio (BPR). Mechanical alloying involved 30-min milling cycles, followed by 30-min pauses to prevent excessive temperature increases within the vials and to reduce the powder from adhering to the milling equipment. The milling duration varied across the experiments, including processing times of 0, 1, 3, 6, 12, 24, 48, and 72 h.

The changes in particle morphology and size were examined using a Zeiss DSM 960A scanning electron microscope (SEM) operating at a voltage of 20-kV voltage. Powder X-ray diffraction (XRD) was employed to identify phase composition and structural/microstructural parameters, using a Philips XPert Bragg–Brentano geometry (θ-2θ) instrument equipped with a CuKα radiation source ($\lambda_{\text{Cu}} = 0.154056$ nm). XRD patterns were recorded in the range of 20–80° with a step size of 0.02°. Phase composition analysis was conducted using ICDD (PDF-2, 2014) and COD-2021 database files. Structural parameters were determined through XRD patterns refinements using the HighScore Plus program (version 3.0.4, Almelo, The Netherlands) based on the Rietveld method [26].

The conventional approach for determining the amorphous fraction involves using the internal standard method. The amorphous phase amount is calculated as the complement to one of the total amounts of crystalline phases [27]. The weight percentage of the amorphous phase present in the sample can be expressed through the following relationship [27]:

$$
W_a = \frac{1}{1 - W_S} \left(1 - \frac{W_S}{W_R} \right) \tag{5}
$$

where W_a is the amorphous fraction, W_S is the weighted internal standard fraction, and W_R is the refined fraction of the internal standard.

Finally, magnetic measurements at room temperature were performed using a vibrating sample magnetometer (VSM, model 3900). This instrument is known for its high sensitivity, capable of detecting changes as small as 0.5 μemu. The magnetic field range for these measurements spanned from $-10{,}000$ Oe to $+10{,}000$ Oe, allowing for a comprehensive evaluation of the magnetic properties of the studied powdered samples.

3 Results and Discussion

3.1 Particles Morphology

3.1.1 Morphology of Milled Powders

Figure 1 presents the evolution of particle morphology and size distribution of the powders as a function of milling time. The morphological changes in the $Ti_{50}Ni_{50}$ powder particles during mechanical milling, which consists of a mixture of face-centered cubic nickel (fcc-Ni) and hexagonal close-packed titanium (hcp-Ti), can be attributed to the differences in mechanical properties between these two metals.

Notably, significant morphological changes are already evident after just 1 h of milling as shown in Figs. 1 and 2 (SEM images 1, 2a, and 2b). Particles become flattened due to plastic deformation induced by progressive forces resulting from ball-powder-ball and ball-powder-jar collisions. The ductile nature of Ni and Ti materials contributes to an increase in particle size as well as the formation of smaller particles [28]. As milling progresses, particle fragmentation becomes dominant over welding, and the amount of amorphous phase increases, leading to increased brittleness of the powders. Consequently, the size of the particles is significantly reduced, and their spherical equiaxial morphology becomes more pronounced.

Eventually, a balance is achieved between the welding rate, which tends to increase the average particle size, and the fragmentation rate, which tends to reduce the average particle size [29].

A characteristic rough structure, typical of laminated plates, is observed in the 1 h milled powder (Fig. 2a). A typical "lamellar" structure featuring alternating layers of Ni and Ti is evident. We examined a particle at $50\times$ and $10\times$ magnification, which revealed several phenomena, such as layer adhesion, fracturing, and cracking. Additionally, the presence of 0.5 to 1-μm holes and small particles of a similar size, which may be associated with these holes, is noticed [30].

It is worth noting that the powders milled for 1 h (Fig. 2b) contain nanoscale particles with broad size distribution in the range 145 to 536 nm. Figure 3 also reveals welding interfaces that are not perfectly bonded, likely due to the roughness of the particle surfaces. However, atoms or nanoclusters can diffuse across these imperfect interfaces, eventually forming well-bonded joints [31]. This diffusion process can lead to a more uniform and cohesive microstructure in the milled powder.

After 3 h of milling, the microstructure of the milled powder undergoes further transformation, as evidenced by the presence of nanoparticles with sizes between 76 and 465 nm, as well as the formation of microcracks that are approximately 5 μm in size (Fig. 4a). These microcracks may form due to the stress imparted during the milling process, which causes particles to fracture or dislocations to move within the material. The formation of these defects leads to an increase in the internal energy of the material, primarily driven by the rise in surface energy [31].

To counteract this increase in internal energy, atoms or nanoclusters redistribute themselves across the surface of the microcracks. This self-healing mechanism works to fill the cracks and mitigate the impact of the defects on the overall microstructure of the milled powder. As the atoms or nanoclusters disperse and fill the microcracks, the overall surface area of the material is reduced, which in turn decreases the driving force for diffusion and stabilizes the internal energy.

The process of microcrack formation and subsequent self-healing provides valuable insight into the material's ability to adapt and evolve during the mechanical milling process. As the material undergoes repeated cycles of fractures, dislocation, and diffusion, the microstructure becomes more refined and cohesive, ultimately resulting in a material with improved mechanical properties and enhanced performance in various applications.

Figure 3 shows, after 3 h of milling, the two phenomena of intensive fracturing (Fig. 3a) and cold welding (Fig. 3b), due to repeated collisions (logs-powder-beads and balls-powder-wall of the bowl) [22].

These phenomena occur due to repeated collisions between the milling media, such as the interactions between the rods, powder particles, beads, and the inner wall of the milling container [30]. The interplay of these forces contributes to the dynamic nature of the milling process, leading to both the breakage and fusion of powder particles.

Following 24 h of milling (Fig. 4b), it can be observed that the milled particles have become smaller in size, with very fine particles appearing on the surface of the aggregates. These fine particles are predominantly located within the cracks that have formed as a result of the continuous milling of the powdered material.

This observation suggests that the milling process has led to a significant reduction in particle size over time. The presence of fine particles on the surface of the aggregates indicates that the milling process has induced a
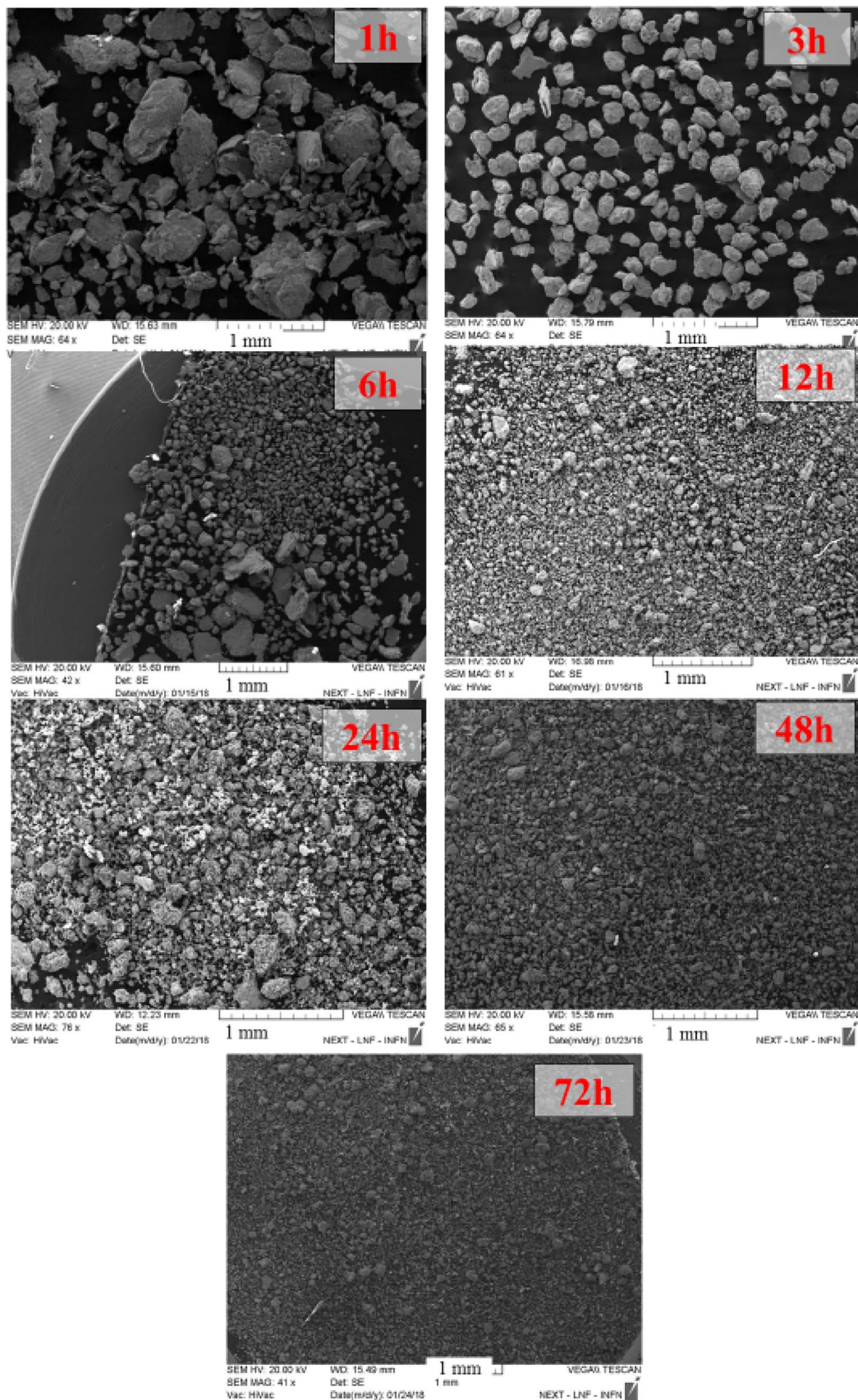
Fig. 1 Evolution of particles' morphology of $Ni_{50}Ti_{50}$ powdered mixture as a function of milling time
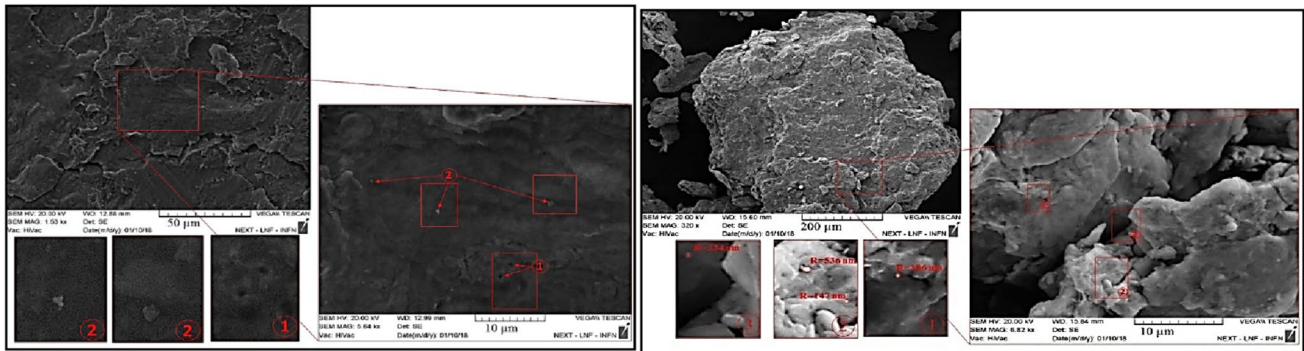
Fig. 2 Particles' morphology after 1 h of milling. **a** General morphology. **b** Welding interfaces that are not perfectly bonded and appearance of nanoparticles

combination of fragmentation and agglomeration phenomena, which have contributed to the evolution of the material's microstructure. The fine particles within the cracks may also play a role in healing these defects, as they can disperse and fill the cracks, leading to a more cohesive and robust microstructure.

After 48 h of milling (Fig. 4c), large agglomerates of very fine particles can be observed, with these particles becoming thinner and smaller as the milling time increases [29]. This indicate that after 48 h of milling, the produced agglomerates are significantly smaller compared to those formed at earlier milling stages. Additionally, the particles within these agglomerates are smaller and more homogeneous than those obtained during previous milling intervals.

For both 48 h (Fig. 4c) and 72 h (Fig. 4d) milling times, a large number of very fine, spherical particles can be observed, with sizes not exceeding 2 μm. Furthermore, a greater quantity of nanoparticles is present compared to the earlier milling stages. The particles forming the agglomerates at 72 h are smaller than those obtained at 48 h.

These observations highlight the continuous refinement and homogenization of the milled material's microstructure as the milling time progresses. The formation of smaller, more homogeneous particles and agglomerates suggests that the material is evolving toward a more uniform and cohesive state.

Figure 4d depicts the smallest particles, which are capable of resisting deformation without fracturing and tend to be welded into larger pieces. These particles combine with other very fine particles to form larger agglomerates with an intermediate size [28]. During the 72-h milling process, the welding phenomenon results in a collection of nanoparticles featuring both circular and longitudinal shapes (Fig. 4d). This is due to the diffusion of atoms or nanoclusters across the surface of the microcracks.

The ability of these small particles to resist deformation and contribute to the formation of larger agglomerates highlights the complex nature of the material's transformation during the milling process. The welding of nanoparticles into various shapes can be attributed to the dynamic interplay of forces acting upon the particles, such as cold welding, fracturing, and agglomeration.

3.2 Analysis of the Chemical Composition by EDX

The primary objective of this section is to verify that a homogeneous distribution of Ni and Ti elements was achieved after milling. It can be noted that the chemical

Fig. 3 Particles' morphology of the powders after 3 h of milling: **a** cold-welding and **b** fracture

(a)   **(b)**

(c)   **(d)**
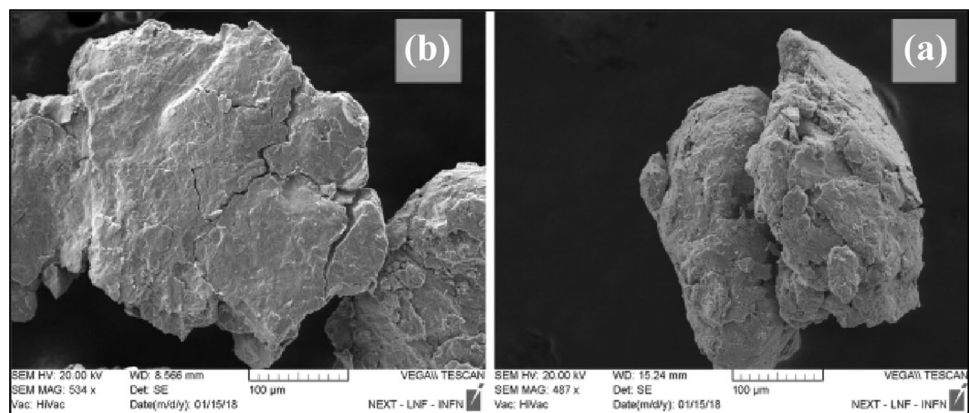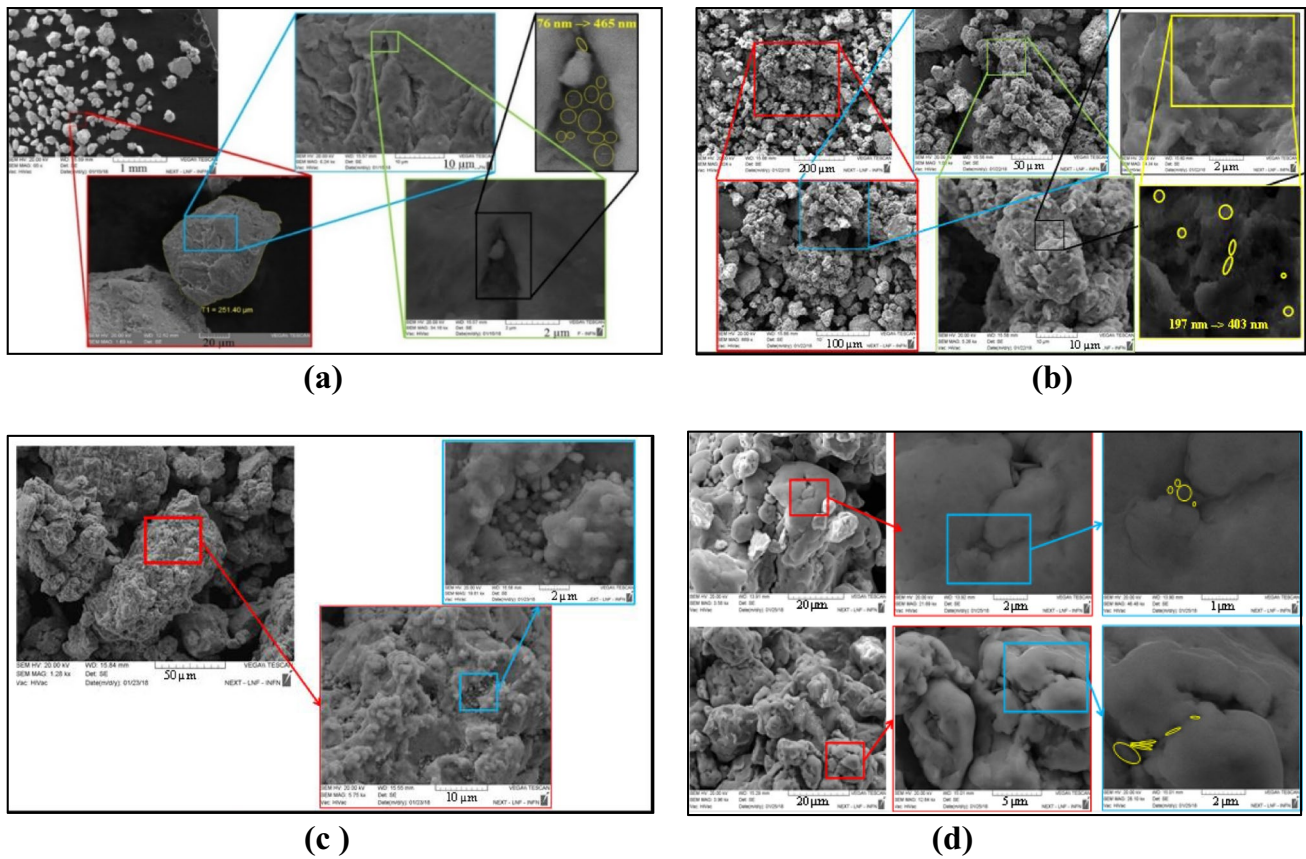
Fig. 4 Particles' morphology as a function of milling. **a** Presence of nanoparticles and formation of micro cracks. **b** 24 h showing the presence of agglomeration of very fine particles. **c** 48 h showing enhanced agglomeration of very fine particles. **d** 72 h showing the welding phenomenon and presence of microcracks

composition of the powder particles exhibits minimal variation between samples. This section also presents the mapping spectra for the Ni and Ti elements, along with elements that may appear due to contamination from milling tools, such as Fe, O, Si, Cr, and C, in the $Ni_{50}Ti_{50}$ system for powders as a function of milling time.

Following 1 h of milling (Fig. 5a), the presence of Ni and Ti is predominantly observed within the analyzed powder particles, while the elements O and C are mainly found on the carbon adhesive tape used to fix the powder on the SEM sample holder. Additionally, the elements Cu and Al are identified and belong to the sample holder.

After a 12-h milling process (as depicted in Fig. 5c), the distribution of Ni and Ti within the powder particles becomes notably more uniform. Additionally, the presence of O and Fe elements is found to have increased, as evidenced by the elemental mapping data. The observed particle size for these elements is approximately 10 μm [32].

The distribution of elements within a single 300-μm particle is illustrated through cartographic analysis and EDS

in Fig. 6a1, following a 12 h milling. The particle welding effect is visible, resulting in the formation of an almost crystalline particle. This may represent a precursor stage to the formation of fully crystalline particles. Examination of the EDS spectrum for this region reveals a well-distributed presence of Ni and Ti elements, along with oxygen (O) and iron (Fe) concentrations of 3.85% and 0.19%, respectively (refer to Fig. 6a1).

Figure 6a2 displays the elemental distribution within a single particle after 48 h of milling, characterized primarily by the aggregation and fusion of numerous fine particles. The cartographic analysis reveals a superior elemental distribution compared to previous findings. As milling time advances, the mixture's homogeneity improves, while the concentrations of O and Fe also increase, likely due to contamination during the milling process (refer to Fig. 6a2).

Figure 6b presents the analysis of a collection of particles (approximately 20 μm in size) after 72 h of milling. A favorable mixture of elements is observed, with Ni and Ti

(a)

(b)

(c)
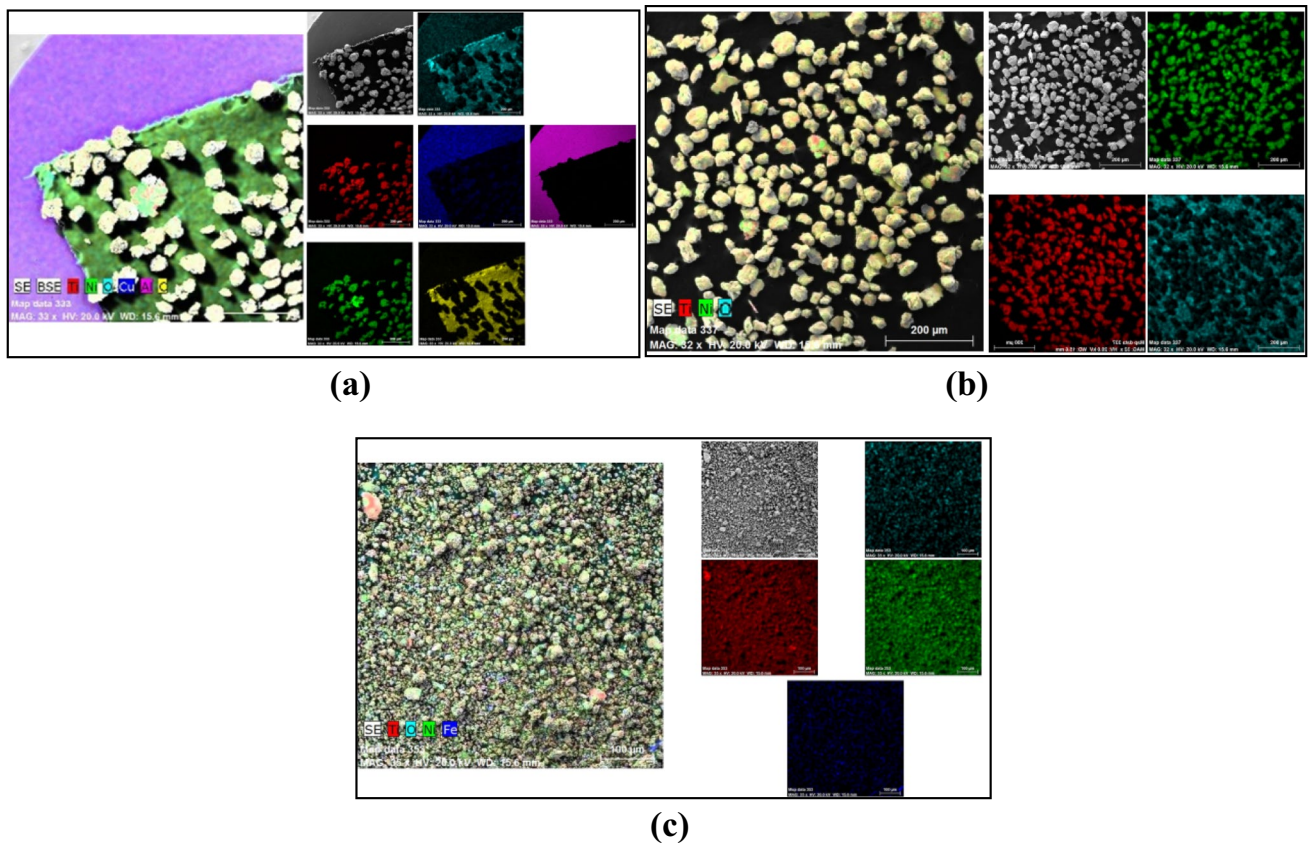
Fig. 5 EDX elemental mapping as a function of milling time: **a** 1 h; **b** 3 h; and **c** 12 h

particle sizes being very small, up to 1 μm. However, larger particles containing Fe, O, and C can reach up to 20 μm. The observed larger carbon particles are attributed to fix the powders onto the SEM sample holder.

The EDS spectrum for this region reveals that the proportions of O_2 and Fe continue to rise (see T Fig. 6b), with these values being significantly higher compared to earlier milling stages. Notably, the Ni and Ti ratios for milling times of 12, 24, 48, and 72 h remain constant, suggesting that the distribution has become more consistent and homogeneous. Based on these observations, it can be concluded that a 12 h milling duration is sufficient to achieve a homogeneous $Ni_{50}Ti_{50}$ powder mixture.

In the given text, Fig. 7 presents the change in the contamination levels of O and Fe in the powder as a function of milling time. A low amount of Fe contamination, likely originating from milling tools such as balls and the vial, is observed. After 72 h of milling, Fe content reaches 1.04% atomic. Iron contamination occurs because of wear debris generated from the vial and balls during the milling process. Additionally, a substantial presence of O impurities is also detected in the milled $Ni_{50}Ti_{50}$ mixture which is likely due to exposure to open air during powder handling.

A portion of this O contamination is adsorbed on the powder's surface, while the rest exists in the form of iron oxides in the ground powder. These iron oxides have not been detected by X-ray diffraction, possibly because their quantity is too low within the diffractometer resolution, as shown in Fig. 10. It is important to note that the percentage of O contamination increases as the milling time increases. This can be attributed to the refinement of particle size in the powders and the high affinity of O to the carbon adhesive. The increase in O contamination over time is supported by the results reported in the literature [32].

The concentration of the starting elements Ni and Ti as determined by EDS analysis, as depicted in Fig. 8, can be divided into three distinct stages:

- The first stage (0–12 h): This phase is marked by a rapid and continuous decrease in the Ni concentration to 42%, while that of Ti concentration increases up to 54%. This can be attributed to the milling process's initial effects on the powder mixture, such as welding and fracture.
- The second stage (12–48 h): During this time interval, the concentrations of Ni and Ti remain almost constant or exhibit only minor fluctuations. The significant deviation

(a1)

(a2)

(b)
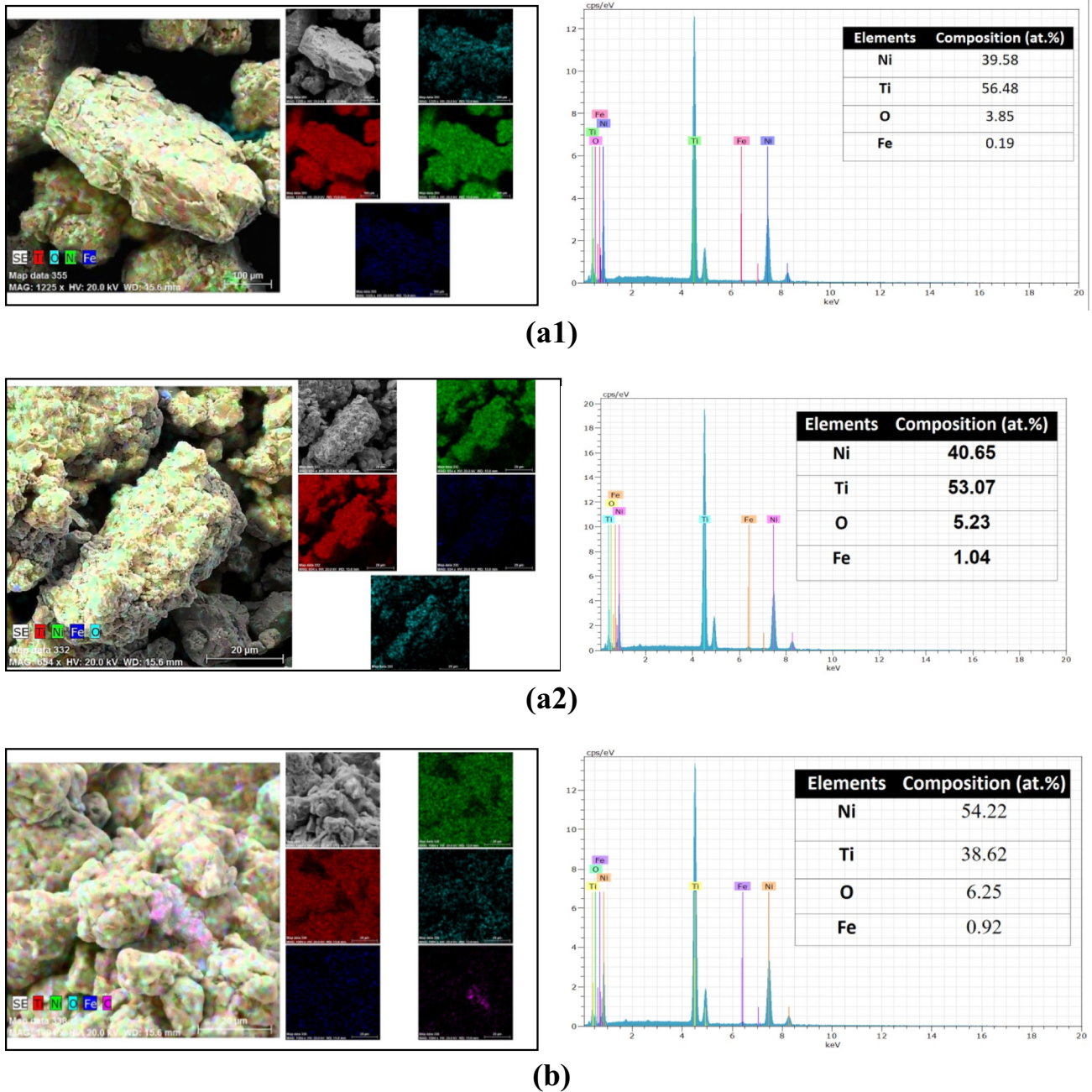
Fig. 6 EDX elemental after milling: **a1**, **a2** 48 h and **b** 72 h corresponding EDX spectrum with the chemical composition as inset

of Ti concentration from its initial composition (50%) could be due to the preferential placement of Ti on particles surface. Ti is known to have a strong affinity for O, and as a result, TiO_2 forms as a passivation layer on particles surface. This phenomenon is particularly notable since SEM resolution only allows for the detection of elements at a depth of approximately 2 μm from the powder's surface.

- The third stage (48–72 h): In this phase, the Ti concentration decreases to 52%, which is directly correlated with the increase in O_2 content (8.88%). This increase in O content is favorable for the formation of an external oxide layer of TiO_2 on particles' surface. The oxide layer's formation may further affect the elemental concentrations detected by the EDS analysis.
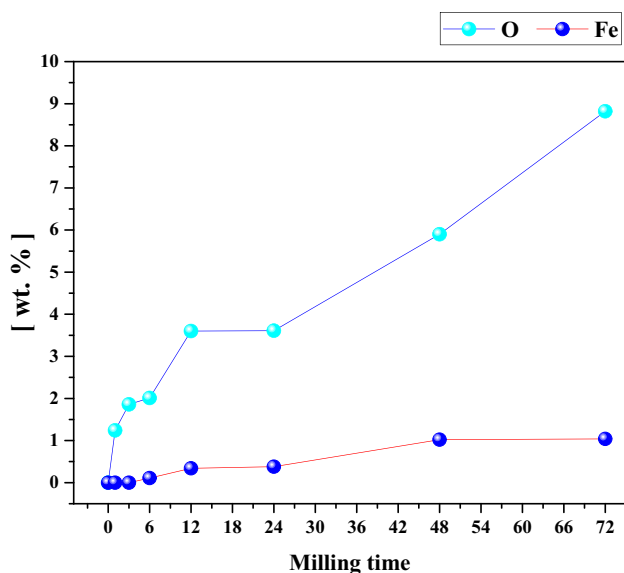
Fig. 7 Evolution of the percentage of contamination of the samples by O_2 and Fe
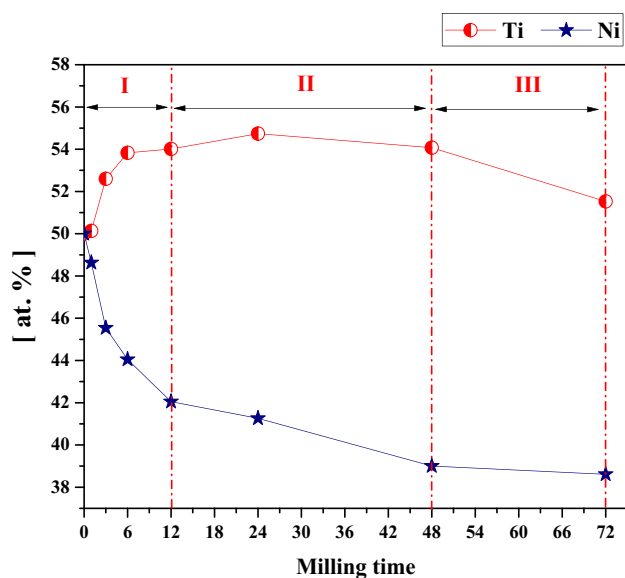
Fig. 8 Concentration of primary elements (Ni and Ti) during milling

3.3 Structural and Microstructural Analyses

The X-ray diffraction (XRD) patterns of $Ni_{50}Ti_{50}$ powders at varying milling intervals (0, 1, 3, 6, 12, 24, 48, and 72 h), as displayed in Fig. 9, show that mechanical alloying leads to notable changes. With the increase in milling time, the peaks broaden consistently, and their relative intensity reduces. This emphasizes the significant influence of the milling process on the disintegration of the starting elemental Ni and Ti powders. These changes can be linked to several processes that occur consecutively [33].

Fig. 9 XRD patterns of $Ti_{50}Ni_{50}$ powder mixture milled for various milling times
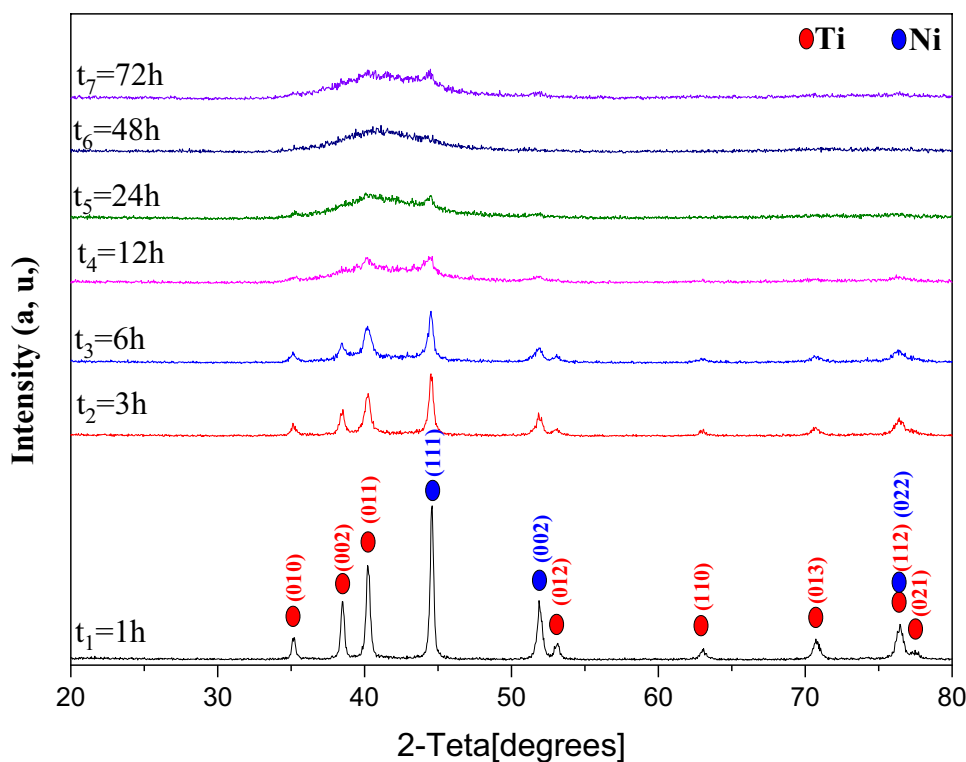
Firstly, particle refinement occurs through the reduction of crystallite size, resulting in smaller particles. This grain refinement contributes to the overall transformation of the material.

Secondly, the introduction of crystalline defects, including vacancies, dislocations, and grain boundaries, takes place. These defects modify the overall structure of the material, influencing its properties and behavior.

Thirdly, as milling progresses, the degree of micro deformations increases due to the substantial amount of energy involved in the milling process. These micro deformations cause additional alterations to the material, further impacting its characteristics.

Lastly, the fragmentation of crystallites and/or the development of the atomic disorder is observed, which in turn also affects the properties of the material. These final changes demonstrate the complexity of the transformations that occur during the milling process.

A thorough examination of XRD patterns have been carried out using the HighScore Plus software [34], the Rietveld refinement [35], and the Warren–Averbach method [36]. This allows for the determination of phase composition, as well as structural and microstructural parameters for each phase (average crystallite size L and microstrain $\sigma^{2\,1/2}$).

The Rietveld refinements of the XRD patterns were performed by analyzing five distinct components: face-centered cubic nickel (FCC-Ni), hexagonal close-packed titanium (HCP-Ti), nickel-titanium austenite (NiTi-As), nickel-titanium martensite (NiTi-Ms), and an amorphous phase. These components are illustrated in Fig. 10.

The production of nanometer-scale diffusion couples is achieved using high-energy mechanical milling, a technique that includes a combination of folding, fracturing, and cold-welding of the milled powders. The milling process generates a large surface area and numerous structural defects, such as dislocations, grain boundaries, and vacancies [22]. These defects facilitate increased atomic diffusivity, which promotes the diffusion and mixing of different atoms. As a result of the improved atomic diffusivity, metastable phases can form during the early stages of the milling process through the solid-state reaction (SSR) mechanism. The formation of these metastable phases occurs at lower temperatures and shorter timescales compared to traditional solid-state synthesis methods. This is attributed to the enhanced diffusion and reaction rates facilitated by the milling-induced defects and increased contact area between the powders.

Throughout the initial three milling stages (1 h, 2 h, and 3 h), the diffraction peaks corresponding to FCC-Ni, HCP-Ti and the amorphous phase persist. However, after 12 h of milling, new diffraction peaks emerge, which are associated with the NiTi-Ms phase, as depicted in Fig. 10 ($t4 = 12$h). During the final three stages of milling (24, 48, and 72 h),

the XRD patterns exhibit the same phases, NiTi-As and NiTi-Ms, but with a predominance of the amorphous phase.

Through the analysis of the Rietveld refinements, comprehensive structural parameters, including symmetry and space group, can be ascertained. Additionally, we can evaluate changes in the content of different phases along, presented as weight percentages, along with average crystallite size L and microstrain $\sigma^{2\,1/2}$, are given in Table 1.

To examine the stability of various phases during mechanical milling, the proportions of the identified phases as a function of milling time are computed in Table 1. In the initial stages of milling, the fractions of mixed elements decrease, which can be attributed to the ongoing dissolution of phases and the formation of solid solutions.

In the 1–6-h period following the formation of the amorphous phase, the decreasing proportions of titanium and nickel are observed to be inversely related to the increasing ratio of the amorphous phase.

After 24 h of milling, the process enters the stage where the formation of martensitic phases starts. During this phase, it is observed that the percentages of the initial elements systematically fluctuate until the HCP-Ti phase disappears entirely. Simultaneously, the growth of the martensitic phase and amorphous phases remains throughout the initial 24 h milling period. The emergence of the martensitic phase can be attributed to the negative mixing enthalpy ($\Delta H = -67$ kJ/mol) [37], which plays a significant role in this transformation.

Upon reaching 48 h of milling, the XRD patterns continue to exhibit the same phases, namely, NiTi-austenite and NiTi-martensite. Nonetheless, a notable shift occurs as the amorphous phase takes precedence, constituting approximately 89% of the relative proportion.

Following 72 h of milling, the ongoing increase in both martensitic and austenitic phases can be attributed to a decrease in the proportion of the amorphous phase. Whereas the formation of martensitic and austenitic phases at milling times of 24 h and 72 h is a result of intense plastic deformations.

As anticipated, with the progression of the milling process, nanocrystallization has emerged, and a considerable amount of lattice strain has accumulated. The presence of two stages in the development of crystallite size and microstrain is typical for materials prepared through high-energy mechanical milling. In the initial milling stage (I: $1 - 24$ h), a significant reduction in crystallite size is achieved, reaching 43.5 nm (6 h), 6.9 nm (24 h), 28.8 nm (12 h), and 101.0 nm (24 h) for Ti-SS, Ni-SS, and M_s, respectively.

In the second stage (II: $12 - 72$ h), a decrease in the crystallite size of the M_s (19.7 nm) and A_s (42.9 nm) phases is observed. Interestingly, the austenite phase displays a significantly larger crystallite size than the martensite
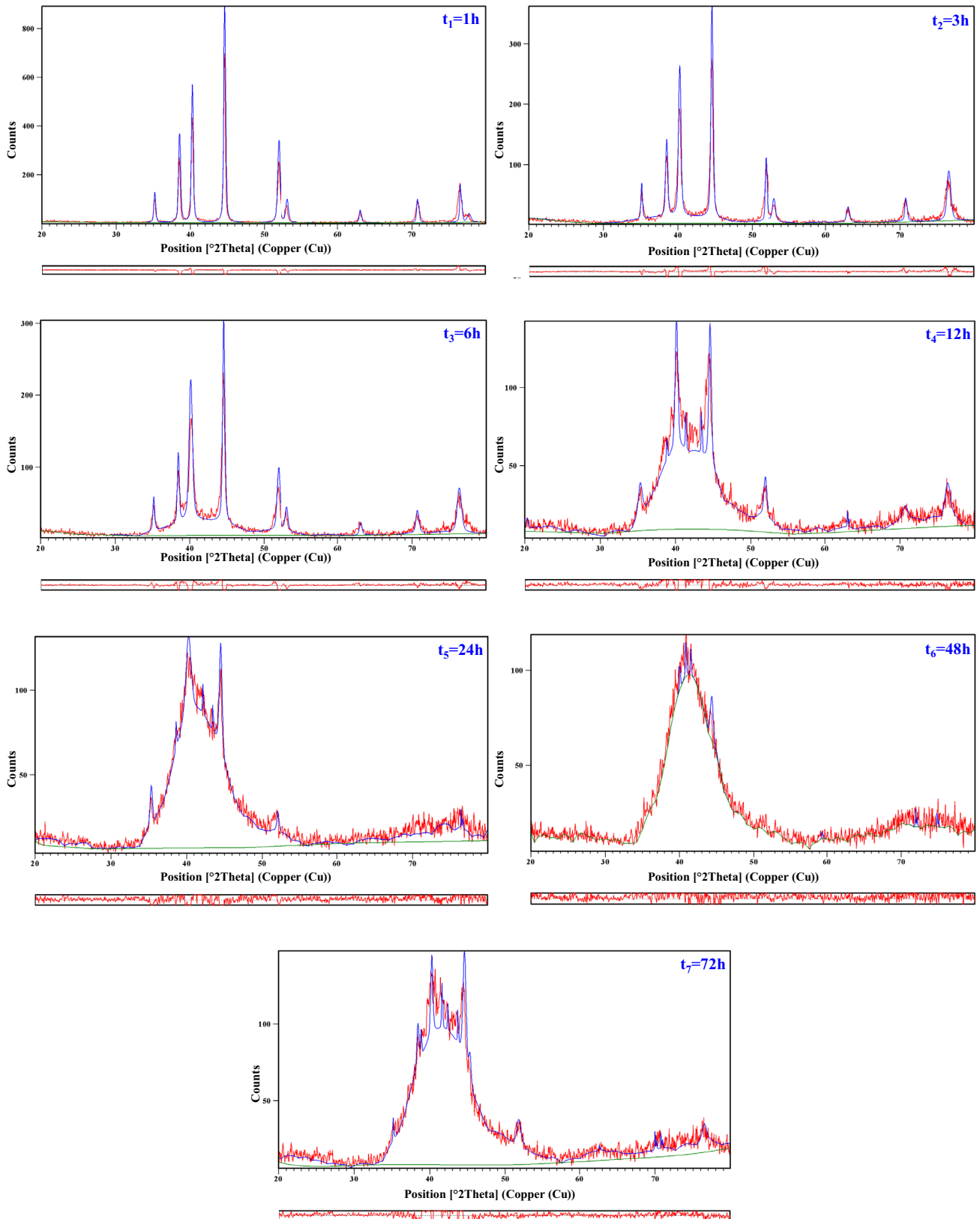
Fig. 10 Rietveld refinements of XRD patterns for milled $Ni_{50}Ti_{50}$ powder mixture

phase, with more than double the size. This reduction in crystallite size can be primarily attributed to the intense particles' deformation during the milling process. Another contributing factor can be the enhanced probability of nucleation sites during crystallization, facilitated by an increased density of defects [38]. The ultimate crystallite sizes are approximately 6.9 nm for FCC-Ni and 29.0578 nm for HCP-Ti. It is also apparent that the decrease in Ni crystallite size occurs more rapidly than in the case of Ti, which is likely related to the smaller initial grain size of FCC-Ni (below 45 μm) compared to HCP-Ti (below 150 μm) [39].
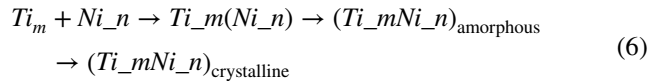
As shown in Table 1, the microstrain $\sigma^{2\,1/2}$ progressively increases as the milling progresses. During the initial milling stage, the microstrain values for Ni-SS, Ti-SS, and Ms reach approximately 0.7442%, 1.2001%, and 0.6014% after 12 h, respectively. This rise in microstrain is typically associated with the growth in dislocation density caused by intense plastic deformations [40]. For NiTi-martensite, the microstrain rises to 0.9534% after 48 h, coinciding with the crystallite size achieving a constant value.

After 72 h of milling, the As phase demonstrates increased microstrains (1.4788%) compared to the Ms phase (1.2132%). This difference can be attributed to the presence of a higher concentration of stacking faults and a greater dislocation density in the As phase. Typically, the microstrain values achieved during the milling process tend to be around 1.5% [41].

During our research on the mechanical alloying (MA) of the $Ti_{50}Ni_{50}$ system, a new reaction route is discovered, which will enrich our understanding of the amorphization process involving Ti and Ni, as well as the formation of A_s and M_s phases.

Building on the comprehensive summary by Suryanarayana in his book on mechanical alloying and milling [23], we observed the following novel pathway in the $Ti_{50}Ni_{50}$ system after 48 h of milling:

$$Ti_m + Ni\_n \rightarrow Ti\_m(Ni\_n) \rightarrow (Ti\_mNi\_n)_{\text{amorphous}}$$
$$\rightarrow (Ti\_mNi\_n)_{\text{crystalline}} \tag{6}$$

In this context, m and n denote the atomic composition of Ti and Ni, respectively. $Ti\_m(Ni\_n)$ symbolizes a solid solution of nickel in titanium $(Ti\_mNi\_n)_{\text{crystalline}}$ signifies a crystalline phase, and $(Ti\_mNi\_n)_{\text{amorphous}}$ represents the amorphous phase with the composition Ti_mNi_n. The discovery of this additional reaction pathway in the $Ti_{50}Ni_{50}$ system after 48 h of milling, which involves the formation of austenite and martensite phases, not only enriches the existing framework of MA but also opens up new avenues for further innovation in the field of materials science.

Table 1 Structural parameters (symmetry and space group), crystallite size L (nm), microstrain $\sigma^{2\,1/2}$ (%), and weight percent (%) of each phase

Milling time (h)		0	1	3	6	12	24	48	72
Phases proprieties									
Ni	Symmetry	Face-centered cubic (FCC)							
	Space group	Fm-3m							
	Crystallite size L (nm)	320.0	75.1	50.8	29.4	18.9	6.9	/	/
	Microstrain $\sigma^{2\,1/2}$ (%)	0.0298	0.0779	0.2039	0.3464	0.7442	1.4901	/	/
	Weight percent (%)	50.0	47.0	41.3	35.6	30.8	16.7	/	/
Ti	Symmetry	Hexagonal close-packed (HCP)							
	Space group	P63/mmc							
	Crystallite size L (nm)	240.5	170.9	104.0	43.5	28.8	/	/	/
	Microstrain $\sigma^{2\,1/2}$ (%)	0.0378	0.2116	0.3504	0.5006	1.2001	/	/	/
	Weight percent (%)	50.0	35.1	23.7	16.9	8.0	/	/	/
NiTi-martensite	Symmetry	Monoclinic							
	Space group	P21/m:b							
	Crystallite size L (nm)	/	/	/	/	101.0	68.0	48.9	19.7
	Microstrain $\sigma^{2\,1/2}$ (%)	/	/	/	/	0.6014	0.7581	0.9534	1.0361
	Weight percent (%)	/	/	/	/	5.7	9.8	6.1	22.0
NiTi-austenite	Symmetry	Body-centered cubic (BCC)							
	Space group	Pm-3m							
	Crystallite size L (nm)	/	/	/	/	/	100.9	79.9	42.9
	Microstrain $\sigma^{2\,1/2}$ (%)	/	/	/	/	/	1.0966	1.4522	1.4988
	Weight percent (%)	/	/	/	/	/	0.8	4.9	8.0
Amorphous	Weight percent (%)	/	17.8	35.1	47.4	55.5	72.7	88.9	69.9

Fig. 11 Hysteresis curve (magnetization M as a function of the applied magnetic field H) and interfacial exchange coupling between a Ni layer and a Ti layer
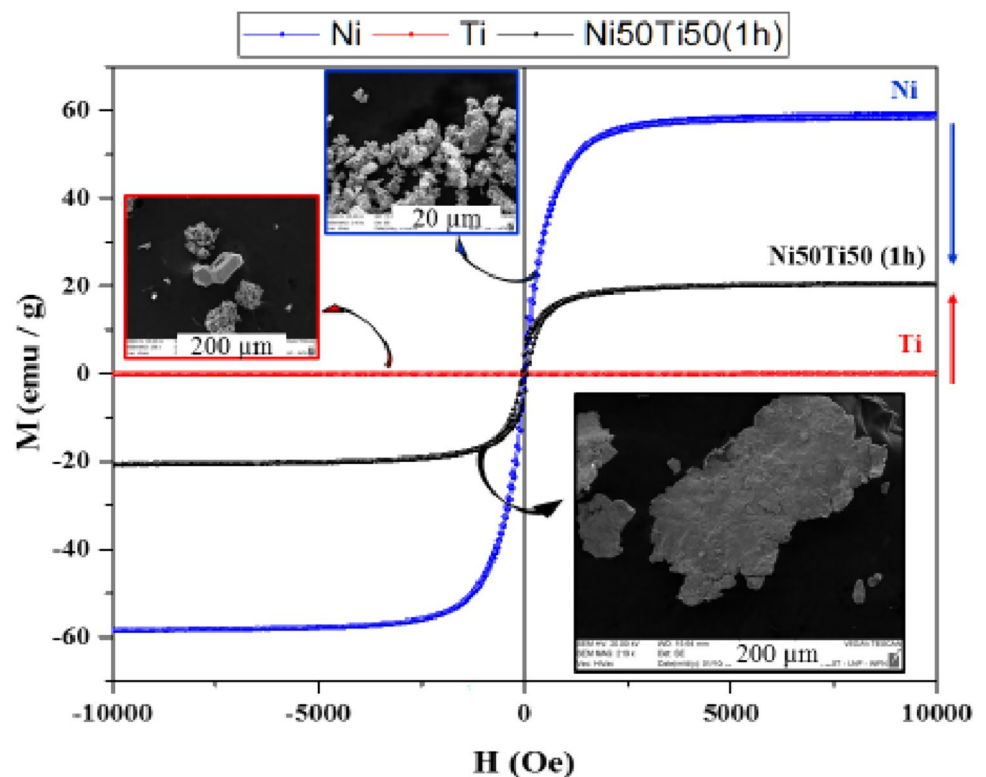
3.4 Magnetic Properties

3.4.1 Hysteresis Cycle Magnetization-Magnetic Field of Pure Elements (Ni and Ti)

Figure 11 depicting the hysteresis curve and Interfacial exchange coupling between a Ni layer and a Ti layer used in milling manifests a narrow curve, typical characteristic of soft ferromagnetic materials. The computed magnetic properties that characterizing nickel are: saturation magnetization $Ms = 58.77$ emu/g, the remanent magnetization $Mr = 3.62$ emu/g, and the coercive field, $Hc = 30.93$ Oe.

Similarly, Ti exhibits a paramagnetic behavior with extremely low values of the saturation magnetization at maximum field $Ms = 0.2652 \ 10^{-3}$ emu/g, the residual magnetization $Mr = 36.90 \times 10^{-3}$ emu/g, and the coercive field, $Hc = 26.76$ Oe close to the values of Ni. In paramagnetic materials, some of the atoms or ions in the material have a permanent magnetic moment due to unpaired electrons in partially filled electronic layers [42].

However, the individual magnetic moments are not magnetically ordered, and the magnetization is zero when the field is removed. In the presence of a field, there is a partial alignment of the atomic magnetic moments in the direction of the magnetic field, which leads to positive magnetization and positive susceptibility.

3.4.2 Interface Interchange Coupling

The shift of the hysteresis loop along the easy axis corresponding to the value of the exchange field and the coherent rotation of the magnetization along the difficult axis shows the interfacial exchange coupling between a Ni layer and a Ti layer (Fig. 11). Nickel exhibits unpaired electrons responsible for magnetic moments and fcc crystal structure with [111] as the hard direction of magnetization. This effect can be explained by changes in the structural and microstructural properties of the ground powder particles.

3.4.3 Magnetization-Magnetic Field Curves (M-H)

A considerable change in magnetic behavior is observed for nanocrystalline ferromagnetic materials compared with conventional counterparts, which strongly depend on several parameters such as chemical composition, phase composition, texture internal crystallography, and particle size.

Figure 12a shows the hysteresis loops (magnetization M concerning the applied magnetic field H) for milled $Ni_{50}Ti_{50}$ milled powders (1, 3, 6, 12, 24, 48, and 72h) measured at ambient temperature. These sigmoidal hysteresis cycles are generally observed in nanostructured materials with small magnetic domains and exhibit a ferromagnetic behavior with a small hysteresis loop. This is due to the presence of structural
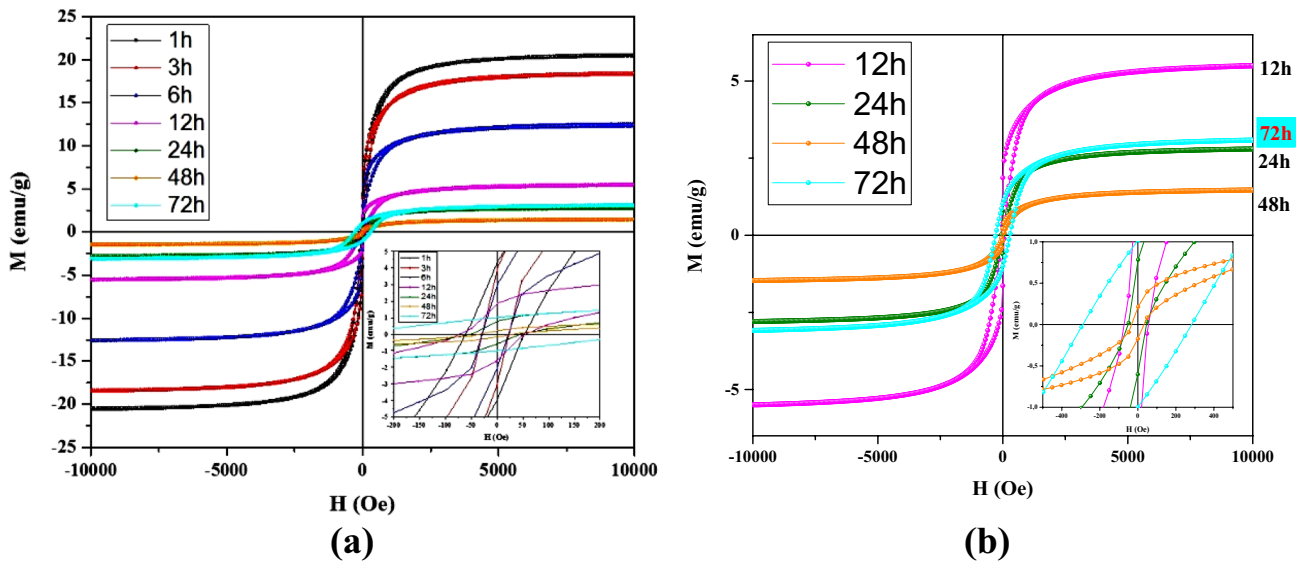
Fig. 12 Hysteresis loops (magnetization M as a function of the applied magnetic field H) for milled $Ni_{50}Ti_{50}$ powders (1, 3, 6, 12, 24, 48, and 72h) measured at ambient temperature **a** full scale and **b** powders milled for (12, 24, 48, and 72h) with inset low-field

distortions within the particles. Small hysteresis losses are properties generally important in soft magnetic materials. It is noted that all the milled powders exhibit a ferromagnetic behavior and that the magnetic properties are very sensitive to the time of milling time, due to following factors:

1. Evolution of phase composition (crystallization of the amorphous phase, formation of new phases, and changes in phase composition)
2. The variations of the lattice parameters of the formed phases due to the formation of SS, nanocrystalline phases, and the amorphous phase.
3. The variation of microstructural parameters, including particle size and micro deformations, combined with the observed reduction in the intensity of the (111) plane with increased milling time, suggests a structural modification due to mechanical milling. This modification may potentially lead to slight ferromagnetic behavior, as observed in the magnetization (M-H) curve. Together, these observations underscore the intricate relationship between changes in microstructure induced by milling and the resultant alterations in magnetic properties.

Note that the width of the hysteresis loops is reduced with the progression of milling time from 1 h to 48 h, then increase suddenly after 72 h (Fig. 12b). The reduction of particle size to the nanoscale involves changes in their magnetic behavior, either in the form of individual particles dispersed in a magnetic or non-magnetic matrix or belonging to particle aggregates [43, 44]. Indeed, this nanoscale of size leads to reconsider some notions such as magnetic domains,

the stability in a time of the direction of magnetization, and the influence of the moments on the surface or by a magnetic anisotropy before the magneto-crystalline anisotropy [45]. The magnetic behavior of nanometric particles, therefore, appears more sensitive than that of massive particles under the influence of external disturbances (magnetic influence of neighboring particles, temperature, external field, and adsorption on the surface).

3.4.4 Variation of the Magnetic Properties as a Function of the Milling Time

The variation of the remanent magnetization, Mr, as a function of the milling time for $Ni_{50}Ti_{50}$ is presented in Fig. 13a. It can be seen that the value of Mr decreases rapidly up to 48 h of milling to reach 0.188 Oe then increases markedly to 1.006 Oe after 72 h of milling. The significant decrease in Mr during the first stage is related of the grain refinement to the nanoscale [46]. Also, it can be correlated with the evolution of the amorphous phase's fraction, hence the absence of a preferred direction for magnetization [46]. The increase in Mr after 72 h is related to the irreversible displacement of magnetic domain walls following the introduction of different types of defects (such as dislocations, grain boundaries, and precipitates) and the increase of the proportion of Ms and As phases at the expense of the amorphous phase (Fig. 13a) [46]. The increase in Mr after 72 h reflects the high value of magnetic anisotropy at the beginning of milling (magnetocrystalline, shaped, and magnetoelastic).

Figure 13b shows the variation of the saturation magnetization, Ms, as a function of the milling time and phase proportion for $Ni_{50}Ti_{50}$ powders. The latter represents the

Fig. 13 Evolution of the magnetic parameters Ni50Ti50 powdered mixture as a function of milling time: **a** remanent magnetization Mr and of phases' proportion, **b** saturation magnetization Ms and of phases' proportion, **c** Coercivity Hc and of phases' proportion, and **d** reduced remanent magnetization (*Mr*/*M*s)
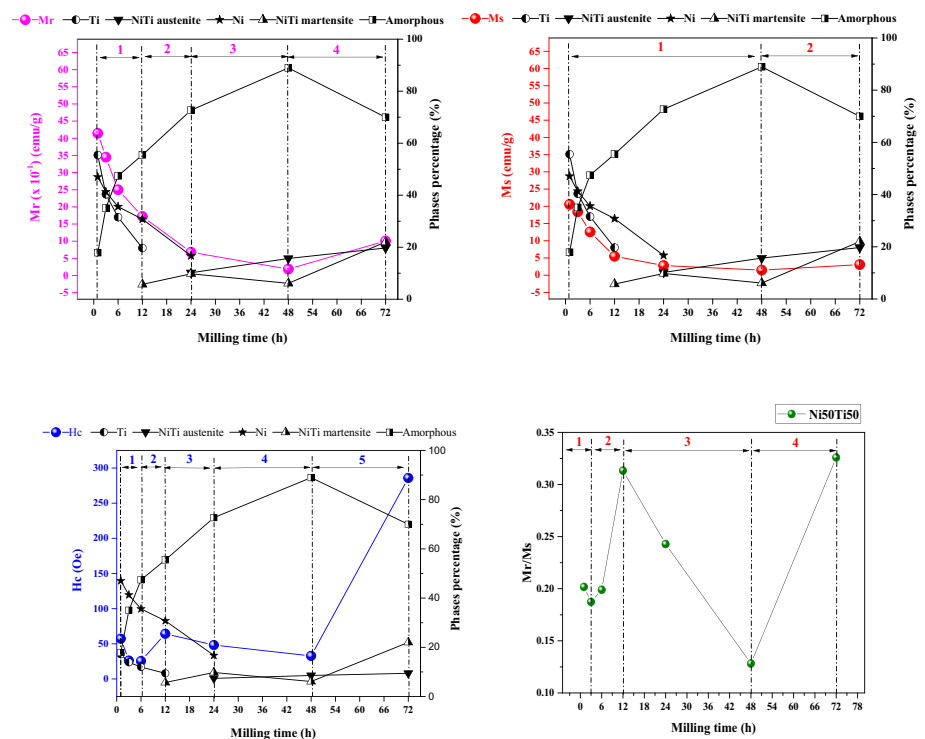
maximum magnetization obtained when all the magnetic moments of the material are aligned in the direction of the applied field. The same trend can be observed for *M*r. The value of *M*s decreases rapidly up to 12 h of milling (5.56 emu/g), then decreases moderately (1.47 emu/g) until 48 h followed by a slight increase at 72 h. The decrease of *M*s during the first stage (from 1 to 48 h) suggests a remarkable change in the magnetic moment (which depends on the atomic coordination or the electronic environment [47]), due to the modification of the crystalline structure and the electronic configuration nearer neighbors of elements Ni and Ti. The structure of nanomaterials can be considered as consisting of two parts: (i) a crystalline nucleus with properties identical to those of massive materials (with structure, mesh parameter, etc.), but these properties are transmitted only at a short distance; (ii) an outer part is formed by the interface (a zone with gaps, defects, impurities, etc.) [43]. The behavior of nanoparticle clusters can be seen as resulting from the interaction of these two types of structures. Local magnetization in the material is determined by the magnetic interaction between adjacent crystallites. This magnetic interaction tries to align the magnetization of all the crystallites in the same direction. The fact that the different crystallites are randomly oriented means that the material has its magnetization in one direction only for a few crystallites and that the magneto-crystalline anisotropy does not have a precise direction [45]. The surface anisotropy energy can have a very important influence since the number of surface atoms becomes important. The surface

anisotropy pushes the magnetic moments in a direction different from that of the inner, thus decreasing the contribution to the magnetization of the nanoparticles [33]. The decrease in *M*s can be explained by the fact that in this field the magneto-crystalline anisotropy is weakened. It is obvious that the variation of the crystallite size and the stress ratio induced by the mechanical milling exhibit saturation. The second stage (48−72 h), is characterized by an increase in the Ms value (from 5.27% after 48 h to 21.58% after 72 h) about a decrease in the amount of the amorphous phase (68.95%) [48]. Thus, it can be deduced from this change that the value of *M*s is only affected by the amorphous phase, the higher the percentage of the amorphous phase, the lower the value of *M*s, and vice versa. This can be associated with the local atomic disorder of the amorphous phase, resulting in no local magnetic moment [49].

The evolution of coercivity (Hc) is primarily influenced by the fabrication conditions, and can be explained by the microstructural evolution affecting the powders during mechanical milling [50]. Figure 13c illustrates the changes in *H*c and phase proportions for $Ni_{50}Ti_{50}$ as a function of milling time, revealing significant changes in the *H*c value. This figure can be divided into five stages. In the first phase (1–6 h), the change in phase proportions affects the *H*c value, resulting in a continuous decrease to 25.43 Oe. The *H*c value's reduction can be attributed to the presence of paramagnetic Ti atoms through the pinning of the magnetic domain walls, the decrease in crystallite size and micro-stresses by the predictions of the random anisotropy model [51], and

the deviation of interatomic spacing in the amorphous phase [52]. In the second phase (6–12 h), the Hc value increases to 64.25 Oe due to the emergence of the martensitic phase (6.36%). The increase in coercivity is also influenced by the internal microstructure and defects produced during milling [33]. During third phase (12–24 h), there is a slight decrease in Hc to 48.27 Oe with a slight increase in the martensite rate (9.05%). This decrease is explained by the emergence of the austenite phase. During the fourth phase (24–48 h), the Hc value continues to decrease to 32.8 Oe, accompanied by a slight decrease in martensite (5.27%) and an increase in austenite (5.45%). The results indicate that the appearance of the austenitic phase contributes to the decrease in Hc. The last phase (48–72 h) is characterized by a sharp increase in the Hc value to 285.8 Oe, due to the decrease may be due to the decrease in the amount of the amorphous phase and the increase in the proportion of the martensitic phase (21.58%). Additionally, the increase in Hc may associated with the fragmentation of magnetic particles during the milling process, leading to a heterogeneous ferromagnetic system where the ferromagnetic grains are rich in Ni. Consequently, the coupling between the ferromagnetic grains becomes less effective, resulting in the observed hardening.

Furthermore, particle size exerts a significant influence on coercivity (Hc), underscored by the crucial role of the mechanical milling process in determining the final dimensions of the particles. This relationship is primarily mediated by the transition from a configuration of multiple magnetic domains (MD) to a single-domain (SD) state as the particle size is reduced [53]. Consequently, the process of mechanical milling becomes indispensable in modulating the magnetic properties of the particles. This modulation is achieved mainly through alterations in particle size, which subsequently influence the structure of the magnetic domains.

The Mr/Ms ratio, known as the reduced remanent magnetization, is a critical parameter from a magnetic perspective. It is used for determining the magnetic energy of a material. Figure 13d depicts the variation of the reduced remanent magnetization as a function of milling time. During the initial 3 h of milling, the reduced remanent magnetization decreases. After that, it experiences a slight increase, reaching a value of approximately 0.1990 after 6 h of milling. After 12 h, the increase becomes more rapid, reaching a value of 0.3133. The observed increase in the Mr/Ms ratio for the Ni$_{50}$Ti$_{50}$ compound after 12 h of milling can be attributed to the irreversible displacement of magnetic domain walls resulting from the creation of numerous defects of various types, such as dislocations and grain boundaries. This increase may also be due to the emergence of nanocrystalline martensite. It is essential to note that materials intended for memory applications must possess sufficient remanent magnetization, meaning the Mr/Ms ratio should approach 1. The Mr/Ms ratio is observed to increase

with milling time, and the obtained values (0.3259 after 72 h of milling) are significantly higher compared to other systems, as mentioned in reference [54]. This indicates that the Ni$_{50}$Ti$_{50}$ compound exhibits promising magnetic properties for memory applications as the milling time progresses.

4 Conclusion

The unveiling of the folding mechanism not only enhances our better understanding of the intricate interactions among various deformation processes in high-energy milling but also presents novel avenues for tunning the properties of nanomaterials and probing their potential applications in sectors such as energy storage, catalysis, and biomedicine.

This study provides a comprehensive analysis of the structural, microstructural, and magnetic properties of nanostructure/amorphous NiTi alloys prepared by mechanical alloying. The unique combination of desirable properties such as shape memory behavior, superelasticity, good corrosion resistance, and biocompatibility make NiTi alloys ideal candidates for various applications in fields such as biomedical, aerospace, automotive, and robotics. The study focused on the influence of processing parameters on the resulting structural, microstructural, and magnetic characteristics of the prepared nanomaterial. The novelty of this research revealed a previously unobserved phenomenon associated with nanomaterial fabrication during high-energy milling processes. The results showed that amorphization and nanocrystallization processes can significantly enhance the properties of NiTi alloys. The average crystallite size L was found to be in the range of 10–20 nm while microstrain $\sigma^{2\ 1/2}$ was found to be in the range of 0.1–0.3%. These findings have significant implications for potential applications in various fields such as biomedical implants. Furthermore, the analysis of magnetic properties indicated that nanostructure/amorphous NiTi milled powders exhibited superparamagnetic behavior at room temperature. This is a unique property that can be exploited for various applications such as magnetic sensors, data storage devices, and biomedical imaging. In summary, this study provides valuable insights into the magnetic and microstructural analyses of nanostructure/amorphous NiTi alloys prepared by mechanical alloying and presents novel avenues for tailoring nanomaterials' properties.

Declarations

Conflict of Interest The authors declare no competing interests.

References

1. Saghaian, S.E. et al. Enhancing shape memory response of additively manufactured NiTi shape memory alloys by texturing and post-processing heat treatment. Shape Memory and Superelasticity. 1–15, (2023)

2. Pu, Z., et al.: Improvement of tensile superelasticity by aging treatment of NiTi shape memory alloys fabricated by electron beam wire-feed additive manufacturing. J. Mater. Sci. Technol. **145**, 185–196 (2023)

3. Liu, M., Zhu, J.-N., Popovich, V.A., Borisov, E., Mol, J.M.C., Gonzalez-Garcia, Y. Passive film formation and corrosion resistance of laser-powder bed fusion fabricated NiTi shape memory alloys. J. Mater. Res. Technol. **23**, 2991–3006 (2023)

4. Yousaf, M. et al. Effect of TiN-based nanostructured coatings on the biocompatibility of NiTi non-ferrous metallic alloy by cathodic cage plasma processing. J Inorg. Organomet. Polym. Mater. 1–13, (2023).

5. Sinha, A. et al. A review on 4D printing of nickel-titanium smart alloy processing, the effect of major parameters and their biomedical applications. Proc. Instit. Mech. Eng., Part E: J. Process Mech. Eng. 09544089231154416, (2023)

6. Sun, F. et al., Brief overview of functionally graded NiTi-based shape memory alloys. Adv. Eng. Mater. 2201434, (2023)

7. Yang, C., Liu, T., Zhong, M., Wu, Z., Deng, J., Du, Y. High recovery stress performance of NiTi shape memory alloy with a wide temperature window. J. Mater. Eng. Perform. 1–13, (2023)

8. Singh, R., Sharma, A.K., Sharma, A.K. Synthesis and characterization of NiTiMDAg nanocomposites for orthopedic applications. J. Mater. Eng. Perform. 1–17, (2023)

9. El-Saies, M.M., Hassan, I., El-Shazly, A.H., El-Wakad, M.T. Titanium foam for dental implant applications: a review. SVU-Intl. J. Eng. Sci. Appl. **4**, nr. 2, 107–112, (2023)

10. Wonneberger, R., Wisniewski, W., Lippmann, S., Müller, F.A., Gräf, S., Undisz, A. Surface amorphization of bulk NiTi induced by laser radiation. Surf. Interf. 102827, (2023)

11. Deng, Z., Huang, K., Yin, H., Sun, Q. Temperature-dependent mechanical properties and elastocaloric effects of multiphase nanocrystalline NiTi alloys. J. Alloys Comp. **938**, 168547, (2023)

12. Nivedita, L.R., Haubert, A., Battu, A.K., Ramana, C.V. Correlation between crystal structure, surface/interface microstructure, and electrical properties of nanocrystalline niobium thin films. Nanomaterials, **10**, nr. 7, 1287, (2020)

13. Ebrahimi, M., Attarilar, S., Gode, C., Kandavalli, S.R., Shamsborhan, M., Wang, Q. Conceptual analysis on severe plastic deformation processes of shape memory alloys: mechanical properties and microstructure characterization. Metals. **13**, nr. 3, 447, (2023).

14. Xu, Y., Sun, Y., Dai, X., Liao, B., Zhou, S., Chen, D. Microstructure and magnetic properties of amorphous/nanocrystalline Ti50Fe50 alloys prepared by mechanical alloying. J. Mater. Res. Technol. **8**, nr. 3, 2486–2493, (2019)

15. Li, F.C., et al.: Amorphous–nanocrystalline alloys: fabrication, properties, and applications. Mater. Today Adv. **4**, 100027 (2019)

16. Ishigami, R., Suzuki, K., Yasunaga, K., Hydrogen desorption characteristics of Mg hydride films with Ni and Ni-based alloy catalyst layers deposited by magnetron sputtering. Thin Solid Films. **764**, 139628, (2023)

17. Yan, B., Jiang, S., Sun, D., Yu, J., Zhang, Y. Comparison for Grain growth dynamics of severely deformed austenite and martensite NiTi shape memory alloys after complete crystallization of amorphous phase. J. Mater. Eng. Perform. **30**, nr. 8, 6191–6202, (2021)

18. Derakhshandeh, M.R., Farvizi, M., Javaheri, M. Effects of high-pressure torsion treatment on the microstructural aspects and electrochemical behavior of austenitic NiTi shape memory alloy. J. Solid State Electrochem. **25**, nr. 1, 279–290, (2021)

19. Yasenchuk, Y. et al. Biocompatibility and clinical application of porous TiNi alloys made by self-propagating high-temperature synthesis (SHS). Materials. **12**, nr. 15, 2405, (2019)

20. Gu, Y.W., et al.: Solid-state synthesis of nanocrystalline and/or amorphous 50Ni–50Ti alloy. Mater. Sci. Eng., A **392**(1–2), 222–228 (2005)

21. Suryanarayana, C.: Mechanical alloying: a critical review. Mater. Res. Lett. **10**(10), 619–647 (2022)

22. Rezgoun, S., Sakher, E., Chouf, S., Bououdina, M., Benchiheub, M., Bellucci, S. Structural, microstructural, and magnetic property dependence of nanostructured Ti 50 Ni 43 Cu 7 powder prepared by high-energy mechanical alloying. J. Superconduct. Novel Magnet. **33**, 2059–2071, (2020)

23. Suryanarayana, C. Mechanical alloying and milling Marcel Dekker. Ee. Uu, 59–78, (2004)

24. Sadrnezhaad, S.K., Arami, H., Keivan, H., Khalifezadeh, R. Powder metallurgical fabrication and characterization of nanostructured porous NiTi shape-memory alloy. Mater Manuf Process, **21**, nr. 8, 727–735, (2006). https://doi.org/10.1080/10426910600727882.

25. Porter, G.A., Liaw, P.K., Tiegs, T.N., Wu, K.H. Particle size reduction of NiTi shape-memory alloy powders, Scripta Materialia, **43**, nr. 12, 1111–1117, (2000). https://doi.org/10.1016/S1359-6462(00)00539-X.

26. Rietveld, H.M.: A profile refinement method for nuclear and magnetic structures. J. Appl. Crystallogr. **2**(2), 65–71 (1969)

27. Bortolotti, M., Lutterotti, L., Pepponi, G. Combining XRD and XRF analysis in one Rietveld-like fitting. Powder Diffraction. **32**, nr. S1, S225-S230, (2017)

28. Loudjani, N., Benchiheub, M., Bououdina, M. Structural, thermal and magnetic properties of nanocrystalline Co 80 Ni 20 alloy prepared by mechanical alloying. J Superconduct Novel Magnet. **29**, 2717–2726, (2016)

29. Arunkumar, S., Kumaravel, P., Velmurugan, C., Senthilkumar, V. Microstructures and mechanical properties of nanocrystalline NiTi intermetallics formed by mechanosynthesis. Intl J Min, Metall. Mater. **25**, 80–87, (2018)

30. Djekoun, A., Otmani, A., Bouzabata, B., Bechiri, L., Randrianantoandro, N., Grenache, J.M. Synthesis and characterization of high-energy ball milled nanostructured Fe50Ni50. Catalysis Today, **113**, nr. 3–4, 235–239, (2006)

31. Hong, S.-J., Suryanarayana, C. Mechanism of low-temperature θ-Cu Ga 2 phase formation in Cu-Ga alloys by mechanical alloying. J. Appl. Phys. **96**, nr. 11, 6120–6126, (2004)

32. Alijani, F., Amini, R., Ghaffari, M., Alizadeh, M., Okyay, A.K. Effect of milling time on the structure, micro-hardness, and thermal behavior of amorphous/nanocrystalline TiNiCu shape memory alloys developed by mechanical alloying. Mater. Design. **55**, 373–380, (2014)

33. Kodama, R.H.: Magnetic nanoparticles. J. Magn. Magn. Mater. **200**(1–3), 359–372 (1999)

34. Degen, T., Sadki, M., Bron, E., König, U., Nénert, G. The high score suite. Powder Diffraction. **29**, nr. S2, pp. S13-S18, (2014)

35. Rietveld, H.M.: Line profiles of neutron powder-diffraction peaks for structure refinement. Acta Crystallogr. A **22**(1), 151–152 (1967)

36. Warren, B., Averbach, B.L. The effect of cold-work distortion on X-ray patterns. J. Appl. Phys. **21**, nr. 6, 595–599, (1950)

37. Li, B.-Y., Rong, L.-J., Li, Y.-Y. Stress–strain behavior of porous Ni–Ti shape memory intermetallics synthesized from powder sintering. Intermetallics. **8**, nr. 5–6, 643–646, (2000)

38. Langford, J.I.: The accuracy of cell dimensions determined by Cohen's method of least squares and the systematic indexing of powder data. J. Appl. Crystallogr. **6**(3), 190–196 (1973)

39. Maziarz, W., Dutkiewicz, J., Van Humbeeck, J., Czeppe, T. Mechanically alloyed and hot pressed Ni–49.7 Ti alloy showing martensitic transformation. Mater. Sci. Eng. A, **375**, 844–848, (2004)

40. Loudjani, N., Gouasmia, T., Bououdina, M., Bobet, J.-L. Phase formation and magnetic properties of nanocrystalline Ni70Co30 alloy prepared by mechanical alloying. J. Alloys Comp. **846**, 156392, (2020)

41. Suryanarayana, C.: Structure and properties of ultrafine-grained MoSi2+ Si3N4 composites synthesized by mechanical alloying. Mater. Sci. Eng., A **479**(1–2), 23–30 (2008)

42. Béranger, G., Duffaut, F., Morlet, J., Tiers, J.-F. A Hundred Years After the Discovery of Invar... the Iron-nickel Alloys. Londres, (1996)

43. Suryanarayana, C.: Nanocrystalline materials. Int. Mater. Rev. **40**(2), 41–64 (1995)

44. Gleiter, H. Nanocrystalline materials. în *Advanced Structural and Functional Materials: Proceedings of an International Seminar Organized by Deutsche Forschungsanstalt für Luft-und Raumfahrt (DLR), Köln, June 1991*, Springer, 1–37, (1991)

45. Liu, J., Shi, M., Lu, J., Anantram, M.P. Analysis of electrical-field-dependent Dzyaloshinskii-Moriya interaction and magnetocrystalline anisotropy in a two-dimensional ferromagnetic monolayer. Phys. Rev. B, **97**, nr. 5, 54416, (2018)

46. Younes, A. Etude par spectroscopie Mssbauer, stabilité thermique et évolution des propriétés magnétiques d'un alliage nanocristallin à base de (FeCo). Annaba, (2012)

47. Gambardella, P. et al. Giant magnetic anisotropy of single cobalt atoms and nanoparticles. Science, **300**, nr. 5622, 1130–1133, (2003)

48. Avar, B., Ozcan, S. Characterization and amorphous phase formation of mechanically alloyed Co60Fe5Ni5Ti25B5 powders. J Alloys Comp. **650**, 53–58, (2015)

49. Mattern, N., Roth, S., Henninger, G., Hermann, H., Eckert, J.: Structural and magnetic properties of amorphous alloys. J. Phys. Condens. Matter **10**(34), L575 (1998). https://doi.org/10.1088/0953-8984/10/34/001

50. Ramakrishna, V.V, Kavita, S., Gautam, R., Ramesh, T., Gopalan, R. Investigation of structural and magnetic properties of Al and Cu doped MnBi alloy. J. Magnet. Magnet. Mater. **458**, 23–29, (2018)

51. Plascak, J.A., Zamora, L.E., Alcazar, G.A.P. Ising model for disordered ferromagnetic Fe− Al alloys. Phys. Rev. B. **61**, nr. 5, 3188, (2000)

52. Gharsallah, H.I., Makhlouf, T., Escoda, L., Suñol, J.J., Khitouni, M. Magnetic and microstructural properties of nanocrystalline Fe-25 at% Al and Fe-25 at% Al+ 0.2 at% B alloys prepared by mechanical alloying process. Eur. Phys. J. Plus. **4**, nr. 131, 1–9, (2016)

53. Lee, J.S., Cha, J.M., Yoon, H.Y., Lee, J.K., Kim, Y.K. Magnetic multi-granule nanoclusters: a model system that exhibits universal size effect of magnetic coercivity. Sci. Rep. **5**, nr. January, 1–7, (2015). https://doi.org/10.1038/srep12135

54. Achour, Y. et al. Solid-state amorphization of a Fe-Co-Nb-B powder mixture by mechanical alloying. în Annales de Chimie, (2010), p. 0.